Title

Key computational findings reveal proton transfer as driving the functional cycle in the phosphate transporter PiPT

Journal

Proceedings of the National Academy of Sciences of the United States of America, 118(25)

ISSN

0027-8424

Authors

Liu, Yu
Li, Chenghan
Gupta, Meghna
et al.

Publication Date

2021-06-22

DOI

10.1073/pnas.2101932118

Peer reviewed

Key computational findings reveal proton transfer as driving the functional cycle in the phosphate transporter PiPT

Yu Liu[a], Chenghan Li[a], Meghna Gupta[b], Nidhi Verma[c], Atul Kumar Johri[c], Robert M. Stroud[b,1], and Gregory A. Voth[a,1]

[a]Department of Chemistry, Chicago Center for Theoretical Chemistry, Institute for Biophysical Dynamics and James Frank Institute, University of Chicago, Chicago, IL 60637; [b]Department of Biochemistry and Biophysics, University of California, San Francisco, CA 94143; and [c]School of Life Sciences, Jawaharlal Nehru University, New Delhi 110067, India

Contributed by Robert M. Stroud, May 6, 2021 (sent for review February 3, 2021; reviewed by José D. Faraldo-Gómez)

Phosphate is an indispensable metabolite in a wide variety of cells and is involved in nucleotide and lipid synthesis, signaling, and chemical energy storage. Proton-coupled phosphate transporters within the major facilitator family are crucial for phosphate uptake in plants and fungi. Similar proton-coupled phosphate transporters have been found in different protozoan parasites that cause human diseases, in breast cancer cells with elevated phosphate demand, in osteoclast-like cells during bone reabsorption, and in human intestinal Caco2BBE cells for phosphate homeostasis. However, the mechanism of proton-driven phosphate transport remains unclear. Here, we demonstrate in a eukaryotic, high-affinity phosphate transporter from *Piriformospora indica* (PiPT) that deprotonation of aspartate 324 (D324) triggers phosphate release. Quantum mechanics/molecular mechanics molecular dynamics simulations combined with free energy sampling have been employed here to identify the proton transport pathways from D324 upon the transition from the occluded structure to the inward open structure and phosphate release. The computational insights so gained are then corroborated by studies of D45N and D45E amino acid substitutions via mutagenesis experiments. Our findings confirm the function of the structurally predicted cytosolic proton exit tunnel and suggest insights into the role of the titratable phosphate substrate.

major facilitator superfamily | phosphate transporter | proton transfer | molecular dynamics

Inorganic phosphate (Pi) is indispensable to life by virtue of its ubiquitous involvement in metabolic processes. The cell uses phosphate transporters to import Pi with the energy provided by either proton or sodium electrochemical potentials across the membrane (1). There has been an increasing interest in high-affinity proton-coupled phosphate transporters, which play an essential role in protozoan parasites (2, 3) and in breast cancer (4) and bone reabsorption (5) in human health. Transporters in the phosphate proton symporter (PHS) family use a proton gradient as the driving force to import phosphate across the plasma membrane of plant cells and fungi. PHS, a family within the major facilitator superfamily (MFS) (6), can provide a necessary perspective on how proton transport (PT) facilitates the substrate transport during the functional cycle of proton-coupled symporters.

The *Piriformospora indica* phosphate transporter (PiPT), purified from a eukaryotic fungus, is the only transporter in the PHS family for which a crystal structure has been determined (7). The stoichiometry factor H^+:Pi of the PHS family varies between 2:1 and ∼4:1 (8–11). PiPT shares high homology with the *Saccharomyces cerevisiae* high-affinity phosphate transporter Pho84 (stoichiometry factor H: Pi 3:1) and with plant phosphate transporters inside the PHS family (*SI Appendix* Table S2). It is a member of the SLC22 family of human organic anion and cation transporters and is homologous to the SLC2 family of glucose facilitative transporters and the related synaptic vesicle 2 protein family of the MFS (7). The only structure of the PHS family to date (Fig. 1*A*) is of a phosphate-bound, "inward-facing occluded (OC)" state and reveals phosphate binding residues together with a cytosolic proton exit tunnel emanating from the binding site. This structure confirms that PiPT, like other transporters in the MFS, has two homologous domains (N and carboxyl domains) each with six transmembrane helices (TMs) related by a quasi-twofold symmetry perpendicular to the membrane plane. Based on the structure, the Stroud group (7) postulated that D324 deprotonation alone triggers phosphate cytosolic release, while D45 and D149 are part of the proton exit tunnel (shown in Fig. 1*A*). Mutagenesis of the highly homologous yeast Pho84 (11–13), in which the D324N (D358N in Pho84) mutant binds phosphate with normal affinity but significantly reduces its transport ability, indicates that D324 is essential for both phosphate transport and PT. The D149N/E (D178N/E in Pho84) mutants reduce half of the phosphate uptake activity while keeping normal binding affinity, which indicates that D149 can be a good candidate residue for proton transfer. The crystal structure of PiPT thus provides a snapshot of the transporter.

In the present work, we have sought to determine how the proton relay occurs and how it is coupled to the phosphate transport. A previous computational analysis (11) of yeast Pho84, starting from an inward open (IO) homology model based on the glycerol 3-phosphate transporter GlpT as template, postulated

Significance

Proton- or sodium-coupled transporters within the major facilitator superfamily are essential for nutrient uptake in all forms of life. We focus on a high-affinity eukaryotic proton-coupled phosphate symporter using extensive classical molecular dynamics (MD) simulations and quantum mechanics/molecular mechanics MD combined with free energy sampling and confirm the role of a key residue, D324, at the molecular level. The results explain the exit direction of the proton once dissociated from D324 and reveal a perspective on proton-coupled transporters, showing that titratable substrates can be involved in the proton transport process as a key aspect of the functional cycle. Mutagenesis and phosphate transport confirm the essential nature of the key D45 residue in the protonation pathway.

Author contributions: Y.L., C.L., M.G., A.K.J., G.A.V., R.M.S., and G.A.V. designed research; Y.L., M.G., and N.V. performed research; Y.L., C.L., M.G., N.V., and A.K.J. analyzed data; and Y.L., C.L., M.G., R.M.S., and G.A.V. wrote the paper.

Reviewer: J.D.F.-G., NIH.

The authors declare no competing interest.

[1]To whom correspondence may be addressed. Email: stroud@msg.ucsf.edu or gavoth@uchicago.edu.

This article contains supporting information online at https://www.pnas.org/lookup/suppl/doi:10.1073/pnas.2101932118/-/DCSupplemental.

Published June 16, 2021.

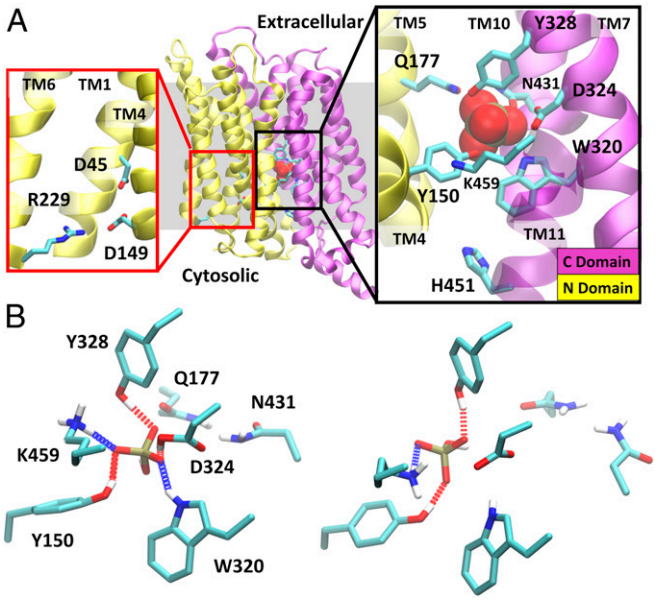

Fig. 1. PiPT crystal structure and phosphate binding interactions. (*A*) PiPT crystal structure (Protein Data Bank 4J05) with enclosed phosphate binding (black box) and proton transfer residues (red box). (*B*) Representative phosphate binding interactions in the OC state (*Left*) and the IO state prior to phosphate exit (*Right*).

that the deprotonation of D149 accompanies the conformational transition from the OC state to the IO state while the Y150 (Y179 in Pho84) side chain acts as its intracellular gate. That computational work protonated only one residue, D149, to form a hydrogen bond with D45 (D76 in Pho84) and found that the docked phosphate remains stable for 30 ns at a putative binding site at least 5 Å further to the cytoplasmic side than in the crystal structure and that upon protonation of D149, Y150 swings back to its OC orientation as in the PiPT crystal structure.

It is known that PiPT uses a proton gradient across the membrane to uptake phosphate; however, the finer details of the phosphate import, binding, and release mechanism remain to be defined. Hence, with the goal of defining which residues govern the coupling of PT to phosphate symport, classical molecular dynamics (MD) simulations were run in the present work starting from the OC state seen as in the crystal structure of PiPT. Multiple protonation assignments were applied to key residues in order to stabilize the OC structure and identify those that produce outward open (OO) and IO conformations. These classical MD simulations provided insight into relative key residue titrations that induce transporter conformational change and phosphate release. In conjunction with enhanced free energy sampling (umbrella sampling), hybrid quantum mechanics/molecular mechanics (QM/MM) was then employed to quantitively define the proton transfer pathways from D324 at the phosphate binding site to D45 both in wild-type PiPT and in the D45N mutant designed to block the pathway through the cytosolic proton exit tunnel. These results demonstrate that the D324 deprotonation event triggers the functional cycle of the transporter through QM/MM MD simulations of explicit proton transfer from D324 to the proton exit tunnel. These simulations yield the result that the phosphate titratable substrate itself participates directly in the PT process in PiPT.

Results and Discussion

Classical Simulations Indicate that the D324 Deprotonation Event Triggers Phosphate Cytosolic Release in which Multiple Proton Transfer Events Proceed in Sequence during the Transition from the OC to the Inward Conformation. In order to analyze whether the PT events in the PT pathway correlate with the conformational transitions, we ran extensive classical MD simulations (see *Methods*) of eight combinations of possible protonation states of titratable residues around the phosphate binding site and compared these between different conformations. First, we sought to determine protonation states of key residues based on the crystal structure of PiPT by calculation with PROPKA (14) and reran the system for multiple OC conformations. D324 was assigned as protonated because of its close contact with negatively charged Pi (Fig. 2 *A* and *B*). Residue D45, the closest protonatable residue to the phosphate binding site (Fig. 1*A*), was assigned as protonated. This agrees with the Pho84 study (11), in which protonated D149 (D178 in Pho84) forms a hydrogen bond with D45, causing the original IO structure to adopt the OC conformation with the gating Y150 orientation restored. Other residues were assigned protonation states based on their calculated pK_a values assuming neutral pH conditions. With this protonation state assignment, both mono- and dibasic Pi were found to interact favorably with K459, D324, Y328, and W320, and the OC structure was stable for more than 1 μs in our classical MD simulations (Figs. 1 *B*, *Left* and 2 *A* and *F*).

Based on mutagenesis of Pho84 (11, 12), in which D324N mutants bind normally but cannot release Pi because of the inability of N324 to deprotonate, we assigned D324 as deprotonated and tested whether this change in D324 protonation alone triggers the conformational transition to the IO state. To our surprise, the PiPT structure transformed to the OO state instead (shown in Fig. 2 *D* and *E*). After careful scrutiny of that structure, we found that H451 (assigned as deprotonated in our previous structures) is the other key residue to phosphate cytosolic release; H451 is the only basic residue beneath the phosphate binding site and above the intracellular edge of the protein and is fully conserved in the entire PHS family. When H451 was assigned as being protonated alongside a deprotonated D324, we observed the expected overall conformational transition from OC to IO state with Pi released into cytosol on a fairly rapid timescale (less than 10 ns; Fig. 2 *B* and *G*).

Consequently, we looked back at the protonation state previously assigned that stabilized the OC structure and reassessed whether it is possible for H451 to be protonated in the OC structure. Further simulations demonstrated that changing only the H451 protonation state does not make a difference—the OC structure is stable for more than 1 μs with Pi remaining inside the binding site (for conformational population distribution, *SI Appendix*, Fig. S4). This finding correlates with our understanding of the transition from the OO state to the IO state. The OO state requires H451 to be deprotonated for the bottom of the Pi binding gate to close, but during the conformational transition to the IO structure, H451 can abstract a proton from nearby water in the Pi binding site and anchor the direction of Pi release. This eliminates the possibility for the Pi to be released prior to the D324 deprotonation event, during which one may expect Pi to be released with D324, D45, and H451 all assigned as protonated in the wild-type PiPT.

Upon deprotonation of D324 and prior to Pi release, both forms of phosphate lose their previous close contact with D324 and W320 (Fig. 1 *B*, *Right*). The contrast between the interaction energies of D324 and W320 with Pi in the OC and IO states shows that the deprotonation of D324 is enough to repel Pi out of the binding site (*SI Appendix*, Table S1); the protonated form of D324 is required to hold Pi at the binding site. The titration of H451, in contrast, has negligible interaction energy differences with Pi because of the relatively large distance (~9 Å) between them. This result confirms the hypothesis (7) that D324 deprotonation is crucial for Pi release. The missing negatively charged residue at the corresponding location of D324 in both of the organic cation and organic anion SLC22 family transporters (15–17) explains why these transporters cannot utilize proton gradient and use sodium gradient instead.

The missing hydrogen bond between Pi and the N7H of W320 prior to Pi release in the IO state suggests that W320 is another

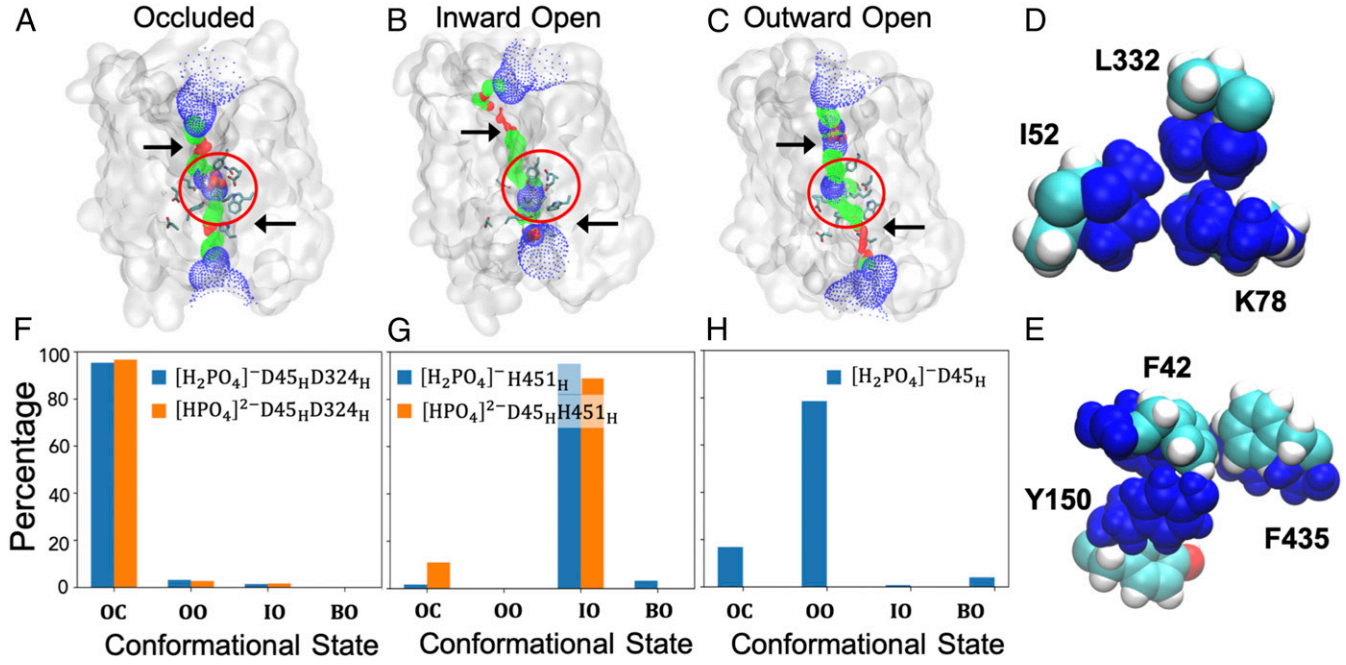

Fig. 2. Population density of states for given combinations of protonation states. Representative structures in the OC (*A*), IO (*B*), and OO (*C*) states. The phosphate binding site is circled in red, and pore radius along the axis perpendicular to membrane plane is plotted in red for smaller than the radius of a water molecule (1.15 Å), blue for larger than the ionic radius of phosphate (2.38 Å), and green for in between. (*D*) Extracellular gate and (*E*) intracellular gate; open in light colors versus closed in dark blue. Arrows indicate the positions of the gates in the structure. *F–H* show the percentage of time spent in each conformation over a time period of ∼1 μs total MD simulation OC, OO, IO, and both gates open (BO). Simulations were for monobasic (blue) or dibasic Pi (orange) for protonation states of residues indicated in each panel. Quantitative measures of different conformational states are defined (*SI Appendix*, Fig. S3). All residues shown are fully conserved in PHS family.

binding residue important to keeping Pi in the OC state. This is probably due to the proximity of W320 to D324 on TM7 and the participation of its bulky side chain in the nearby hydrophobic intracellular gate. The SLC22 family transport anions, cations, and zwitterions. The highly conserved W320 and Y328 residues in the SLC22 family transporters (7) suggest a similar substrate-binding mechanism, particularly using W320 TM7.

Intracellular and Extracellular Gate Opening and Closing. The dominant conformational form and relative probabilities were determined for each protonation state of residues and of the substrate by MD simulations for ∼1 μs each. The open/closed nature of the extracellular and intracellular gates, as depicted in Fig. 2, were defined quantitatively (*SI Appendix*, Fig. S3) and used to quantitate the percentage of time spent in different conformational states. The relative populations show that once D324 is deprotonated but H451 remains neutral, monobasic Pi is repelled by negatively charged D324 and no longer restrained by H451, and it exits to the extracellular space. This again confirms that the protonated form of D324 is essential to retaining Pi at the binding site. The intracellular gate is composed of bulky hydrophobic residues Y150, F42, and F435 beneath the Pi binding site that are fully conserved across the PHS family. Among these, Y150 most clearly participates in gating the channel in the MD simulations. In IO states, deprotonated D324 repels Pi and pushes it from the top of Y150, while protonated H451 beneath Y150 pulls Pi from below. Y150 then alters its sidechain orientation to give way to Pi and open the sealed hydrophobic gate (shown in Fig. 2*E*). Our findings confirm the role of Y150 as a key part of the gate. Mutations (11) that are similarly large hydrophobic Y150F or polar Y150S support the transport of phosphate, while small hydrophobic Y150A and Y150G mutants do not, presumably because of some structural collapse in the latter cases.

QM/MM Simulations Together with D45 Mutagenesis Find that the Exit Path of the D324 Proton Requires D45. During this process, Pi acts as a "transfer station" in between these two aspartic acids. While the departure of the proton from D324 triggers Pi release and conformational transition, D45 participates in transferring this proton to the cytosol through the PT tunnel, as suggested by the pKa calculation of D45 in our OC state classical MD simulations. We observed two typical orientations of protonated D45 in the OC state simulations shown in Fig. 3 *A* and *B*. Protonated D45 can either orient downward to form a hydrogen bond with D149 or orient upward, pointing to Pi. Interestingly, in apo-OO state simulations, the same protonated D45 always hydrogen bonds with D149 and never flips up toward the phosphate binding site. To understand the correlation of proton transfer and D45 sidechain behavior, we calculated the pKa of D45 with PROPKA separately on frames of OC state trajectories displaying different orientations of the D45 side chain. The predicted pKa of D45 with either downward- or upward-oriented side chain corresponds to 7.7 ± 0.6 and 5.9 ± 0.5, respectively. These results suggest that the D45 side chain orients downward in the OO state, and, once Pi has been imported to the binding site, D45 transfers its proton to cytosol, and then its side chain reorients toward Pi for reprotonation from the Pi. As shown in Fig. 3*D*, the water connectivity between D45 side chain and Pi, D45 side chain and D149 side chain illustrates that pathways of hydration are maintained throughout. This supports the proposal of the PT tunnel that allows transport of the proton from Pi to D45 and eventually to cytosol via D149 and R229.

To fully address questions such as where the D324 proton transports and whether Pi titration happens during the process, we explored this problem in a more quantitative manner and calculated the free energy profile (potential of mean force [PMF]) for the PT process from D324 to D45 using umbrella sampling free energy sampling (18) in QM/MM MD simulations (19, 20). The

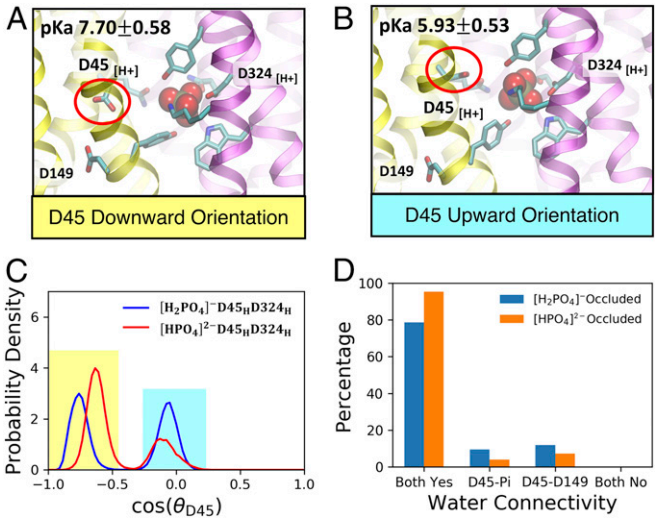

Fig. 3. D45 as a proton transfer residue. (*A* and *B*) Typical D45 orientations in the OC state structure. (*C*) The bimodal distribution of D45 side chain orientation in the OC states. $\cos(\theta_{D45})$ quantitively describes D45 side chain orientation, in which negative value represents D45 side chain pointing below the *x-y* plane. The angle θ_{D45} is defined as the angle between z-CA-CG. (*D*) Water connectivity probability between D45-phosphate and D45-D149 in OC states.

reaction coordinate, also called the collective variable (CV), was defined as

$$CV = \vec{r}_{\mathrm{CEC-Pi}} \cdot \frac{\vec{r}_{\mathrm{D324-D45}}}{|\vec{r}_{\mathrm{D324-D45}}|}, \qquad [1]$$

where center of excess change (CEC) is the excess proton center of excess charge (21) located originally on D324 and Pi is the center of mass of the phosphate. The D324 and D45 subscripts in that CV equation denote the center of mass of the carboxylic three terminal heavy atoms of the side chain. The primary advantage of this reaction coordinate (CV) design is that it does not bias the titration of Pi while still permitting water titration within four solvation shells of the CEC (21).

For the initial QM/MM umbrella sampling window, we chose representative snapshots from the classical MD simulations with protonated D324 and deprotonated D45 assigned. Even though the CV does not drive Pi titration in either direction, we still observed explicit proton transfer from D324 to both forms of Pi and eventually to D45 via Grotthuss proton shuttling through water molecules present in wild-type PiPT after ∼100 ns equilibration. This result is fascinating in the sense that, to our knowledge, no previous transporter simulation has observed substrate titration itself as being crucial to enable the functional cycle. It is thus possible that other transporters of titratable substrates might also change their protonation state and therefore their chemical and physical properties midway through the transport process. The excess proton remained on D324 in the lowest free-energy state, shown as "a" for both forms of Pi in Fig. 4 *A* and *B*. Then, when the proton is transferred to Pi, the previously dibasic phosphate becomes monobasic and contributes to a local free energy minimum at "b" in Fig. 4 *A*, *Upper*. The previously monobasic phosphate, on the other hand, transforms to H_3PO_4, and this emerges as the transition state of the PT process. The proton comes to the side chain of D45 in both systems via shuttling through water molecules, and this forms the corresponding local free energy minimum in both PMFs. The overall proton transfer process in both mono- and dibasic phosphate systems has a kinetic barrier of around 7 kcal/mol, and the time constant (inverse of the rate constant) for both processes is thus less than 5 ns, which matches the classical MD computational observation of the phosphate release time scale in the IO state. The overall barrier to PT through dibasic Pi is slightly lower than that for monobasic Pi. These results therefore support the proposed phosphate release steps depicted in Fig. 5.

In order to further validate the role of titratable D45, we performed another parallel set of QM/MM MD umbrella sampling simulations for the D45N mutant, which mimics the irreversibly protonated D45, and compared the corresponding PMFs with those of the wild type depicted in Fig. 6. In contrast to the barrier height of the wild type (WT) PMFs in Fig. 4, those of the D45N mutant have barriers higher than 15 kcal/mol, and the mutant PMFs show no apparent local minimum in the vicinity of the D45N side chain (<2Å). The shapes of the PMFs of both systems are similar during the PT process from D324 to both forms of phosphate, but they show a major difference in the subsequent step of the mechanism in which the proton is passed to D45(N) via water proton shuttling. Because of the nonprotonatable nature of the N45 residue, there is no local free energy minimum at N45 (contrasted with protonated D45) in the mutant PMF. These two findings support our hypothesis based on classical MD simulations that D45 is the starting point of the PT tunnel and should be deprotonated first to receive the proton from D324. The proton transfer tunnel lining along the direction of the proton gradient across the membrane, with D149 immediately transferring a proton from D45 to bulk, can provide a constant driving force for the excess proton leaving D324 moving toward D45.

Experimental mutagenesis followed by growth (Fig. 7) also demonstrates the essential nature of D45 for phosphate release. The D45N mutant has ∼10-fold lower K_m and 5-fold lower V_{max} compared with wild-type PiPT, showing that the nontitratable D45N mutant binds phosphate but does not transport it as well. The mutant D45E that preserves the charge allows the same K_m but lowers the V_{max} by a further 10-fold (50-fold below wild type). Classical MD simulations of D45E with corresponding protonation state assignments of the WT OC states show that it induces a structural collapse (*SI Appendix*, Fig. S5). A new turn is formed in helix 4 below D149 (in dark blue) that severely disrupts the phosphate binding environment compared to WT and D45N

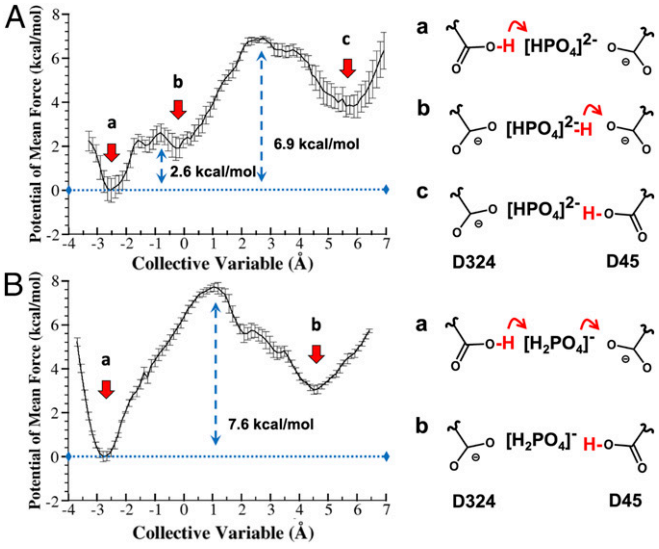

Fig. 4. PMF from QM/MM MD for the proton transfer process from D324 to D45 mediated by phosphate (dibasic phosphate for *A*; monobaisc phosphate for *B*) at the binding site. Vertical red arrows represent thermodynamic stable states depicted on the right column. The activation free energy barrier along the reaction coordinate (CV) is marked in blue.

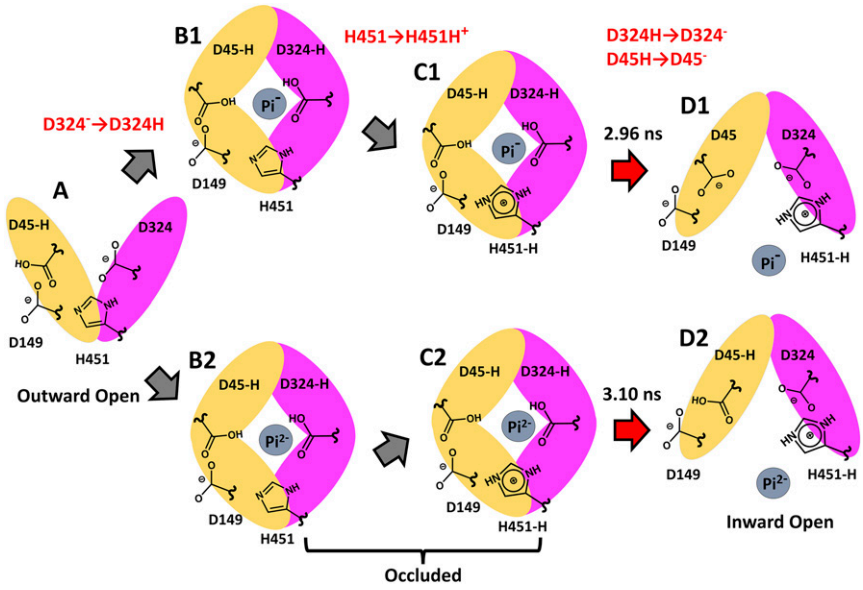

Fig. 5. Deduced mechanism of how proton transfers couple conformational changes to phosphate transport: (*A*) Stabilized OO state. (*B1, 2*) Stabilized OC states either with monobasic or dibasic phosphate in the primary binding site. (*C1, 2*) Intermediate states lead to protonation of H451. (*D1, 2*) Stable IO state accompanies phosphate release (either monobasic or dibasic) and deprotonation of D324. Arrows represent inferred proton transfer processes from classical MD simulations, while the ones in red have the proton transfer timescale calculated as the inverse of the transfer rate constant calculated by transition state theory and QM/MM MD PMF calculations.

mutants, which may explain the diminished phosphate uptake rate in D45E mutant.

Based on our classical and QM/MM MD simulations, here we propose the overall proton transfer pathway through conformational transitions as follows: D45 is initially protonated. During phosphate import from the apo-OO state to the OC state, one proton binds to D324 to hold either form of Pi at the binding site, and another proton protonates H451 that stabilizes the negative charge on Pi (state A to state Cs in Fig. 5). Phosphate release begins with the deprotonation of D45 to the intracellular side. The proton of D324 moves to the phosphate and eventually is passed to D45 (state Cs to state Ds). Because of the proton gradient across the membrane, this second proton on D45 exits the PT tunnel to reach the cytosol either before the cytosolic departure of monobasic Pi or after the cytosolic departure of dibasic Pi. The proton on H451 leaves to the intracellular side upon recycling of the transporter from IO to OC, proceeding on to the OO state. As a result, the stoichiometry factor H^+:Pi for PiPT functional cycle is estimated to be 3:1, which fits into the range of stoichiometry factors experimentally observed across the entire PHS family.

Here, it should be clarified that it is, ultimately, the balance of electrochemical potentials at either side of the membrane that drives the direction of the functional cycle. When we say that proton transfer reactions drive the functional cycle, we are stressing the coupling relationship between proton and phosphate transport during the phosphate cytosolic release. We did assume the reversibility of the phosphate extracellular release during the conformational transition from the OC to the OO state. Thus, we marked the reverse process in Fig. 5 and inferred the protonation of D45 and D324 upon the import of phosphate. We suggest that a codependence of proton and phosphate transfer can exist when the electrochemical potential difference from both sides of the membrane shifts sign. A two-dimensional PMF with one CV describing the proton transfer process and the other CV defining the phosphate release could more fully address this issue. However, because of the computationally demanding nature of QM/MM, this result is exceedingly hard to obtain at present.

Conclusions

In this work, we justify at a detailed molecular level the hypothesis that the deprotonation of the key residue D324 triggers phosphate

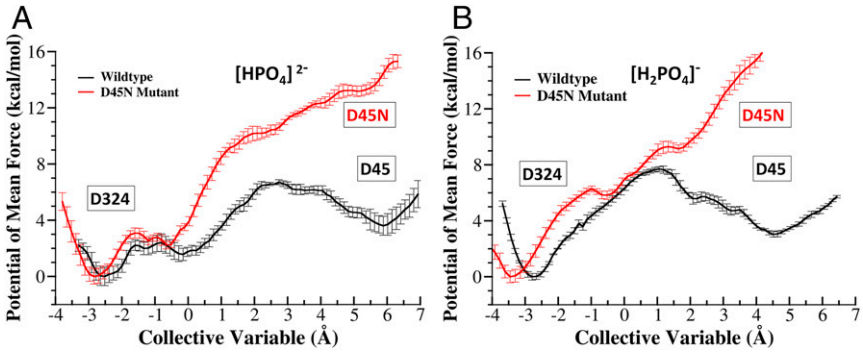

Fig. 6. QM/MM MD PMF comparison for the proton transfer process from D324 to D45 in wild-type PiPT (black) and D45N mutant (red). (*A*) Proton transfer PMF for dibasic phosphate at the binding site. (*B*) PMF for monobasic phosphate at the binding site (*SI Appendix, Methods*).

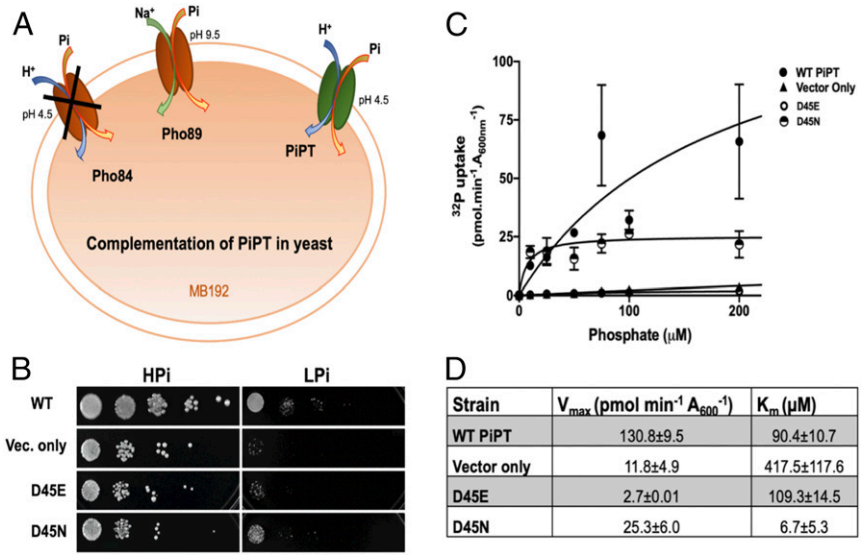

Strain	V_{max} (pmol min^{-1} A_{600}^{-1})	K_m (μM)
WT PiPT	130.8±9.5	90.4±10.7
Vector only	11.8±4.9	417.5±117.6
D45E	2.7±0.01	109.3±14.5
D45N	25.3±6.0	6.7±5.3

Fig. 7. Mutagenesis identifies D45 as a key proton transfer residue in the functional cycle of PiPT. (*A*) A pictorial representation of high-affinity phosphate transporters in *Saccharomyces cerevisiae*. Pho84 is absent in MB192 and complemented by PiPT WT or the D45 mutants. (*B*) Growth assay showing serial dilutions (from optical density at 600 nm ($O.D._{600nm}$) 0.3 and 10× serial dilutions) of the cells in high- (HPi) and low-phosphate (LPi) conditions on minimal media agar plates. (*C*) Michaelis–Menton curves for the phosphate transport assay of PiPT D45E and D45N. (*D*) Values of K_m and V_{max} derived from curve fitting (GraphPad Prism 6) are tabulated.

release. Our work combines results from classical MD simulations and QM/MM MD–free energy sampling to successfully answer the questions of where and how the proton on D324 travels vectorially across the membrane during the phosphate release process. The quantitative QM/MM PMFs confirm D45 as the starting residue of the PT tunnel and offer a perspective on proton-coupled transporters in which titratable substrates such as phosphate may be explicitly involved in the PT process as a key part of driving the functional cycle. Our design of an appropriate CV together with QM/MM MD simulations proves to be critical to the study of such complicated systems with multiple titratable sites along the transport pathway.

Methods

Classical MD simulations were run for the PiPT crystal structure (Protein Data Bank ID code 4j05) embedded in a solvated dimyristoylphosphatidylcholine lipid bilayer to simulate the biological environment. The disordered residues from 230 to 296 between N and carboxyl domains in the crystal structure were not simulated; however, we assume this does not affect the function of PiPT within the MFS based on the Pho84 and LacY deletion experimental results (22–25). The models were built in the CHARMM-GUI web server (26, 27) following standard equilibration protocols. Protonation states were assigned based on PROPKA (14) calculations. The CHARMM-CMAP and CHARMM 36 force field (28–30) were employed to describe the protein, lipid, and ligand interactions. Simulations with the choices of the protonation states of the system with phosphate release were replicated (from the same starting structure but with different velocity assigned) three times with GROMACS MD software (31). Principal component analysis on the trajectories is shown (*SI Appendix*, Fig. S6). QM/MM MD simulations for the wild-type PiPT were initiated from a structure with D324 protonated, D45 deprotonated, and H451 protonated equilibrated in classical NPT simulations for at least 100 ns. Similarly, the D45N mutant was simulated with the same D324 H451 protonation states. The QM/MM simulations were performed in the CP2K package (32). The QM region was described by density functional theory with the Becke Lee–Yang–Parr (BLYP) functional (33, 34) and the D3 dispersion correction (35, 36). The free energy profile (PMF) for PT from D324 to D45/N45 were then calculated with QM/MM umbrella sampling by tracking the excess proton CEC (21) relative to phosphate along the direction from D324 to D45 side chain oxygens. The proton transfer rate constant was then estimated using transition state theory. Details of the calculation of the PT rate are found in the *SI Appendix*. Further details of the simulation set up are also contained in the *SI Appendix*.

Data Availability. All study data are included in the article and/or *SI Appendix*. Previously published data were used for this work (structures of PiPT and mutants are deposited in the Protein Data Bank as 4J05).

ACKNOWLEDGMENTS. This research was supported by the National Institute of General Medical Sciences of the NIH through Grants R01 GM053148 (to G.A.V.) and R01 GM24485 (to R.M.S.). A.K.J. is thankful to the Department of Biotechnology, Government of India for financial support through TATA Innovation fellowship. Computing facilities were used that were provided by the Extreme Science and Engineering Discovery Environment, which is supported by NSF Grant OCI-1053575, and by the University of Chicago Research Computing Center. We thank Professor Jessica Swanson (University of Utah) and Dr. Zhi Yue for helpful discussions on the likely protonation state of H451 in PiPT. We thank Dr. Janet Finer-Moore for structural biology interpretations.

1. M. Gu, A. Chen, S. Sun, G. Xu, Complex regulation of plant phosphate transporters and the gap between molecular mechanisms and practical application: What is missing? *Mol. Plant* **9**, 396–416 (2016).
2. T. Russo-Abrahão *et al*., Transport of inorganic phosphate in *Leishmania infantum* and compensatory regulation at low inorganic phosphate concentration. *Biochim. Biophys. Acta* **1830**, 2683–2689 (2013).
3. T. Russo-Abrahão *et al*., H^+-dependent inorganic phosphate uptake in *Trypanosoma brucei* is influenced by myo-inositol transporter. *J. Bioenerg. Biomembr.* **49**, 183–194 (2017).
4. M. A. Lacerda-Abreu *et al*., H^+-dependent inorganic phosphate transporter in breast cancer cells: Possible functions in the tumor microenvironment. *Biochim. Biophys. Acta Mol. Basis Dis.* **1865**, 2180–2188 (2019).
5. M. Ito *et al*., Characterization of inorganic phosphate transport in osteoclast-like cells. *Am. J. Physiol. Cell Physiol.* **288**, C921–C931 (2005).
6. S. S. Pao, I. T. Paulsen, M. H. Saier Jr, Major facilitator superfamily. *Microbiol. Mol. Biol. Rev.* **62**, 1–34 (1998).
7. B. P. Pedersen *et al*., Crystal structure of a eukaryotic phosphate transporter. *Nature* **496**, 533–536 (2013).
8. C. I. Ullrich-Eberius, A. Novacky, E. Fischer, U. Lüttge, Relationship between energy-dependent phosphate uptake and the electrical membrane potential in *Lemna gibba* G1. *Plant Physiol.* **67**, 797–801 (1981).
9. C. I. Ullrich-Eberius, A. Novacky, A. J. E. van Bel, Phosphate uptake in *Lemna gibba* G1: Energetics and kinetics. *Planta* **161**, 46–52 (1984).
10. K. Sakano, Proton/Phosphate stoichiometry in uptake of inorganic phosphate by cultured cells of *Catharanthus roseus* (L.) G. Don. *Plant Physiol.* **93**, 479–483 (1990).
11. D. R. Samyn, J. Van der Veken, G. Van Zeebroeck, B. L. Persson, B. C. G. Karlsson, Key residues and phosphate release routes in the *Saccharomyces cerevisiae* Pho84 transceptor: The role of Tyr179 in functional regulation. *J. Biol. Chem.* **291**, 26388–26398 (2016).
12. D. R. Samyn *et al*., Mutational analysis of putative phosphate- and proton-binding sites in the *Saccharomyces cerevisiae* Pho84 phosphate:H(+) transceptor and its effect on signalling to the PKA and PHO pathways. *Biochem. J.* **445**, 413–422 (2012).

13. S. A. Ceasar, A. Baker, S. P. Muench, S. Ignacimuthu, S. A. Baldwin, The conservation of phosphate-binding residues among PHT1 transporters suggests that distinct transport affinities are unlikely to result from differences in the phosphate-binding site. *Biochem. Soc. Trans.* **44**, 1541–1548 (2016).
14. M. H. M. Olsson, C. R. Søndergaard, M. Rostkowski, J. H. Jensen, PROPKA3: Consistent treatment of internal and surface residues in empirical pK_a predictions. *J. Chem. Theory Comput.* **7**, 525–537 (2011).
15. M. A. Hediger *et al*., The ABCs of solute carriers: Physiological, pathological and therapeutic implications of human membrane transport proteinsIntroduction. *Pflugers Arch.* **447**, 465–468 (2004).
16. R. Fredriksson, K. J. V. Nordström, O. Stephansson, M. G. A. Hägglund, H. B. Schiöth, The solute carrier (SLC) complement of the human genome: Phylogenetic classification reveals four major families. *FEBS Lett.* **582**, 3811–3816 (2008).
17. A. Schlessinger *et al*., Comparison of human solute carriers. *Protein Sci.* **19**, 412–428 (2010).
18. G. M. Torrie, J. P. Valleau, Nonphysical sampling distributions in Monte Carlo free-energy estimation: Umbrella sampling. *J. Comput. Phys.* **23**, 187–199 (1977).
19. T. Laino, F. Mohamed, A. Laio, M. Parrinello, An efficient real space multigrid QM/MM electrostatic coupling. *J. Chem. Theory Comput.* **1**, 1176–1184 (2005).
20. T. Laino, F. Mohamed, A. Laio, M. Parrinello, An efficient linear-scaling electrostatic coupling for treating periodic boundary conditions in QM/MM simulations. *J. Chem. Theory Comput.* **2**, 1370–1378 (2006).
21. C. Li, J. M. J. Swanson, Understanding and tracking the excess proton in *Ab Initio* simulations; Insights from IR spectra. *J. Phys. Chem. B* **124**, 5696–5708 (2020).
22. E. Bibi, H. R. Kaback, *In vivo* expression of the *lacY* gene in two segments leads to functional *lac* permease. *Proc. Natl. Acad. Sci. U.S.A.* **87**, 4325–4329 (1990).
23. K. H. Zen, E. McKenna, E. Bibi, D. Hardy, H. R. Kaback, Expression of lactose permease in contiguous fragments as a probe for membrane-spanning domains. *Biochemistry* **33**, 8198–8206 (1994).
24. A. B. Weinglass, H. R. Kaback, The central cytoplasmic loop of the major facilitator superfamily of transport proteins governs efficient membrane insertion. *Proc. Natl. Acad. Sci. U.S.A.* **97**, 8938–8943 (2000).
25. F. Lundh *et al*., Molecular mechanisms controlling phosphate-induced down-regulation of the yeast Pho84 phosphate transporter. *Biochemistry* **48**, 4497–4505 (2009).
26. S. Jo, T. Kim, V. G. Iyer, W. Im, CHARMM-GUI: A web-based graphical user interface for CHARMM. *J. Comput. Chem.* **29**, 1859–1865 (2008).
27. J. Lee *et al*., CHARMM-GUI input generator for NAMD, GROMACS, AMBER, OpenMM, and CHARMM/OpenMM simulations using the CHARMM36 additive force field. *J. Chem. Theory Comput.* **12**, 405–413 (2016).
28. J. B. Klauda *et al*., Update of the CHARMM all-atom additive force field for lipids: Validation on six lipid types. *J. Phys. Chem. B* **114**, 7830–7843 (2010).
29. R. B. Best *et al*., Optimization of the additive CHARMM all-atom protein force field targeting improved sampling of the backbone φ, ψ and side-chain $\chi(1)$ and $\chi(2)$ dihedral angles. *J. Chem. Theory Comput.* **8**, 3257–3273 (2012).
30. J. Huang *et al*., CHARMM36m: An improved force field for folded and intrinsically disordered proteins. *Nat. Methods* **14**, 71–73 (2017).
31. M. J. Abraham *et al*., GROMACS: High performance molecular simulations through multi-level parallelism from laptops to supercomputers. *SoftwareX* **1-2**, 19–25 (2015).
32. T. D. Kühne *et al*., CP2K: An electronic structure and molecular dynamics software package - Quickstep: Efficient and accurate electronic structure calculations. *J. Chem. Phys.* **152**, 194103 (2020).
33. C. Lee, W. Yang, R. G. Parr, Development of the Colle-Salvetti correlation-energy formula into a functional of the electron density. *Phys. Rev. B Condens. Matter* **37**, 785–789 (1988).
34. A. D. Becke, Density-functional exchange-energy approximation with correct asymptotic behavior. *Phys. Rev. A Gen. Phys.* **38**, 3098–3100 (1988).
35. S. Grimme, J. Antony, S. Ehrlich, H. Krieg, A consistent and accurate ab initio parametrization of density functional dispersion correction (DFT-D) for the 94 elements H-Pu. *J. Chem. Phys.* **132**, 154104 (2010).
36. J. Klimeš, A. Michaelides, Perspective: Advances and challenges in treating van der Waals dispersion forces in density functional theory. *J. Chem. Phys.* **137**, 120901 (2012).